Journal of Power Sources 573 (2023) 233009

Contents lists available at ScienceDirect

Journal of Power Sources

journal homepage: www.elsevier.com/locate/jpowsour

Nonlinear identifiability analysis of Multiphase Porous Electrode Theory-based battery models: A Lithium Iron Phosphate case study

Giacomo Galuppini, Marc D. Berliner, Daniel A. Cogswell, Debbie Zhuang, Martin Z. Bazant, Richard D. Braatz *

Massachusetts Institute of Technology, Cambridge, MA 02139, USA

HIGHLIGHTS

- First identifiability analysis for Multiphase Porous Electrode Theory-based models.
- The analysis is carried out for discharge data from a lithium iron phosphate battery.
- The analysis identifies which parameters cannot be estimated from the data.
- The lack of identifiability is explained in terms of the battery physics.
- Approaches are proposed for removing the lack of parameter identifiability.

ARTICLE INFO

Keywords:
Lithium-ion batteries
Lithium Iron Phosphate
Graphite
Multiphase Porous Electrode Theory
Parameter estimation
Identifiability analysis

ABSTRACT

Porous electrode theory (PET) is widely used to model battery dynamics by describing electrochemical kinetics and transport in solid particles and electrolyte. Standard PET models rely on black-box descriptions of the thermodynamics of active materials, typically obtained by fitting an open-circuit potential which does not allow for a consistent description of phase-separating materials. Multiphase PET (MPET) was recently developed to describe batteries using white- or gray-box descriptions of the thermodynamics with additional parameters that need to be estimated from experimental data. This work analyzes the identifiability of parameters in the MPET model, including the standard kinetics and diffusion parameters, as well as MPET-specific parameters for the free energy of active materials. Based on synthetic discharge data, both linearized and nonlinear identifiability analyses are performed for an MPET model of a commercial Lithium Iron Phosphate/Graphite battery, which identify which model parameters are not identifiable and which are identifiable only with large uncertainty. The identifiable parameters control phase separation, reaction kinetics, and electrolyte transport, but not solid diffusion, consistent with rate limitation by intercalation reactions at low rates and by electrolyte diffusion at high rates. The article also proposes approaches for reducing parameter identifiability issues.

1. Introduction

Lithium-ion batteries are the leading technology for energy storage for a huge range of devices (e.g., laptops, cell phones, electric vehicles), and for smart grid applications [1,2]. Several lines of research focus on optimizing battery design and management to enable fast charging, minimize degradation, and improve safety, with the final goal of improving the end-user experience [3–6]. Optimization and management tasks typically leverage mathematical models of the battery [7–9]. Depending on the specific task, physics-based models of different levels of complexity may be required, ranging from simplified, equivalent circuit models to complex, electrochemical based models [10–13]. Moreover, data-driven models are also gaining attention in the literature [14–16], including for the modeling and prediction of battery performance degradation [13,17–19]. Physics-based and data-driven modeling approaches can also be combined as proposed in [20]. Among physic-based models, Porous Electrode Theory (PET) represents a well consolidated modeling tool [21]. PET models electrochemical kinetics at the solid-electrolyte interfaces in porous electrodes, with transport at the continuum scale and particle reactions and diffusion at the mesoscale. This description involves a set of parameters, whose values are typically determined by regressing the model parameters over experimental charge/discharge data [22–24]. On the other hand, the thermodynamics is modeled by an algebraic function for the open-circuit potential which is directly fit to experimental data, with a black-box approach.

* Corresponding author.
E-mail address: braatz@mit.edu (R.D. Braatz).

https://doi.org/10.1016/j.jpowsour.2023.233009
Received 20 January 2023; Received in revised form 11 March 2023; Accepted 25 March 2023
Available online 4 May 2023

In general, when dealing with a parameter estimation problem, it is important to quantify the extent for which model parameters can be estimated from the available data, to be able to make conclusions based on the model parameters and to quantify uncertainties in the model predictions. This quantification can be formalized by carrying out a *parameter identifiability* analysis. Broadly speaking, a parameter is said to be *unidentifiable* if several different values of the parameter produce very similar model outputs. Moreover, parameter (un)identifiability may be related to the values of the other model parameters. Several works in the literature investigate the identifiability issue from a *structural* [25,26] or a *practical* perspective [25,27–29], focusing on different model families (e.g. equivalent circuit [28] or single-particle models [30]), and on different battery chemistries (e.g., $LiFePO_4$ [29], NCA [31], $LiCoO_2$ [32]). The identifiability analysis for the PET model has been carried out [29,31], with Ref. [31] proposing a nonlinear, global identifiability analysis employing a Monte Carlo Markov Chain (MCMC) approach [33,34] and a nonlinear local analysis carried out by direct inspection of two and three-dimensional parameter confidence regions [35].

While PET represents a standard in lithium-ion battery modeling, recent works underline that it is not completely suitable to describe thermodynamics of multiphase active materials, due to the black-box approach adopted to model thermodynamics. For this reason, PET was recently extended to form Multiphase PET (MPET), [36–38], which adopts a white- or gray-box description of the system thermodynamics, thus enabling a description of multiphase phenomena. The main aim of this article is to perform a detailed local identifiability analysis for an MPET model of Lithium Iron Phosphate (LFP) batteries. The analysis is based on both a *linearized* approach, and a local nonlinear analysis of identifiability of couples and triplets of parameters by visual inspection of confidence regions. While the former approach is less computationally expensive, and represents a standard, baseline approach in the literature, the latter is typically more suitable for highly nonlinear systems as electrochemical models, and provides further insight into the identifiability. Following the main contribution, the analysis pays particular attention to the parameters defining the thermodynamic behavior of active materials. Standard transport and kinetics parameters are also included in the analysis, which is performed by relying on an MPET model of A123 System's *APR18650M1A* Lithium Iron Phosphate (LFP) batteries, to ensure relevance of the results to practical applications.

The paper is organized as follows: Section 2.1 provides background on MPET and its relationship to PET; Section 2.2 summarizes the parameter identification methodology, while Section 2.3 summarizes linear and nonlinear approaches for parameter uncertainty quantification. The methodology adopted in this article to examine parameter identifiability is discussed in Sections 2.4 and 2.5. The results of the analysis are presented in Section 3, and further discussed in Section 4. Finally, Section 5 summarizes the main findings of this work.

2. Materials and methods

2.1. Multiphase porous electrode theory

Lithium-ion batteries are typically built using two porous electrodes and a porous separator between them. Each porous electrode consists of several different materials including electrolyte and active material intercalation, binder and conductive additive. During discharge, the lithium contained in the active material of the negative electrode migrates towards the active material of the positive electrode, while undergoing several transport and electrochemical reaction processes. PET [21] represents a well-established approach to model this complex dynamic behavior. In PET, the behavior of the active material is treated by modeling a single representative particle for each electrode, while transport of lithium ions between active particles in the electrolyte is described by Stefan–Maxwell concentrated solution theory. In each electrode, solid active material and electrolyte are coupled by Butler–Volmer (BV) kinetics. Finally, solid transport is modeled as Fickian diffusion. Typically, PET models fall in the category of *pseudo-two-dimensional* (P2D) models, where the position between the two metal contact points on the opposite sides of the battery represent the main dimension, while the distance from the center of a solid particle represents the second, "pseudo" dimension.

A number of software implementations are currently available [39–46]. Among these, some [43,44] are based on freely available modeling languages, while others [45,46] require commercial software or modeling languages.

While PET has been developed and tested for a variety of battery materials, it relies on *empirical* models of the thermodynamics of the active materials, typically obtained by fitting one or more Open Circuit Voltage (OCV) versus State Of Charge (SOC) measurements. This model does not allow the description of active materials with multiple stable phases, except by empirical modifications, such as artificial "shrinking core" [47] or "shrinking annulus" [48] phase morphologies, which unavoidably mask the true thermodynamic behavior of intra-particle [49–57] and inter-particle [38,58–60] phase separation. Recently, MPET [36,37] was developed to model multiphase materials by modeling the free energy functional, rather than the voltage directly, and consistently defining electrochemical activities, overpotentials, and reaction rates [61]. MPET also improves the description of the solid-state dynamics by relying on multiple, interacting particles, placed both along the length of the electrode and also in parallel with each other in terms of electrolyte access. Size and conductance values of individual particles are drawn from suitable lognormal distributions. Moreover, several particle shapes (spheres, cylinders, or rectangular approximation of platelet particles, reacting on the b plane only) and active particle models (e.g., homogeneous, Allen–Cahn or Cahn–Hilliard Reaction models [61–63]) can be considered for the two electrodes [36,61]. In addition, MPET also allows several choices of reaction kinetics, ranging from the empirical Butler–Volmer typically adopted in PET, to Marcus theory of electron transfer and its generalizations [64–67]. Finally, the electrolyte can be specified either as a dilute model or using a full Stefan–Maxwell concentrated solution theory [36]. Many experiments involving optical or X-ray imaging have directly validated this modeling approach [37,38,49–61,68], which is freely available to the public as a Python software. Specifically, the details of the Python implementation of MPET are discussed in [36], where all the equations are provided in full. The software is also provided open source to the public at https://github.com/TRI-AMDD/mpet.

2.2. Parameter estimation: Maximum a posteriori and maximum likelihood

Consider a source of experimental data $\mathbf{y}$ given by

$$\mathbf{y} = S(\boldsymbol{\theta}^*) + \boldsymbol{\epsilon} \tag{1}$$

where $\boldsymbol{\theta}^*$ is the true, unknown value of the parameter of the system S, and $\boldsymbol{\epsilon}$ is stochastic measurement noise. Due to the stochastic nature of $\boldsymbol{\epsilon}$, experimental data needs to be treated as realizations of a (vector) random variable $\mathbf{Y}$. In turn, when trying to estimate the value of $\boldsymbol{\theta}^*$, the model parameter $\boldsymbol{\theta}$ is also treated as a (vector) random variable. Both $\mathbf{Y}$ and $\boldsymbol{\theta}$ are therefore characterized by suitable Probability Density Functions (PDFs).

Given a set of observations for $\mathbf{Y}$ and any available prior information about the parameters $\boldsymbol{\theta}$, Bayesian inference relates the joint distribution of parameters and experimental data, conditioned over experimental data, $P(\boldsymbol{\theta}|\mathbf{Y})$, to the distribution of parameters $P(\boldsymbol{\theta})$ by means of Bayes Theorem [33]:

$$P(\boldsymbol{\theta}|\mathbf{Y}) = \frac{P(\mathbf{Y}|\boldsymbol{\theta})P(\boldsymbol{\theta})}{P(\mathbf{Y})} \tag{2}$$

where $P(\mathbf{Y}|\boldsymbol{\theta})$ is the joint distribution of parameters and experimental data, conditioned over parameters, $P(\mathbf{Y})$ is the distribution of experimental data, $P(\boldsymbol{\theta}|\mathbf{Y})$ is the *posterior* distribution, $P(\boldsymbol{\theta})$ is the *prior*

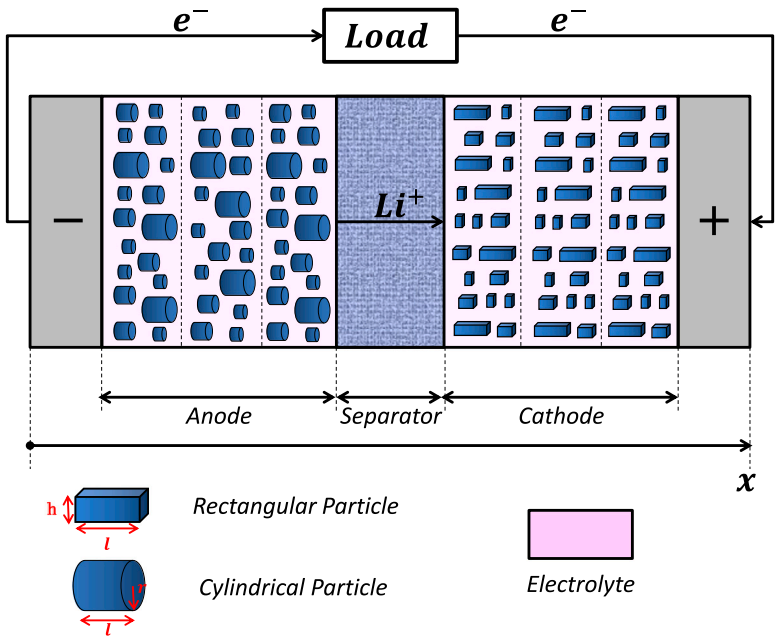

Fig. 1. Schematic of the MPET model for a LFP/graphite cell during discharge.

distribution, and $P(\mathbf{Y}|\boldsymbol{\theta})$ is the *likelihood*. The term $P(\mathbf{Y})$ is a normalizing constant to ensure (2) integrates to 1. *Maximum A Posteriori* (MAP) estimation sets $\boldsymbol{\theta}^*$ as the value that maximizes the posterior probability:

$$\hat{\boldsymbol{\theta}}^{MAP} = \arg\max_{\boldsymbol{\theta}} P(\boldsymbol{\theta}|\mathbf{Y}). \tag{3}$$

When no prior information about parameters is available, $P(\boldsymbol{\theta})$ can be set to a constant, non-informative value. In this case,

$$P(\boldsymbol{\theta}|\mathbf{Y}) \propto P(\mathbf{Y}|\boldsymbol{\theta}) \tag{4}$$

and maximization of the posterior distribution corresponds to maximization of the likelihood function. The parameter estimate for this *Maximum Likelihood* (ML) approach is given by

$$\hat{\boldsymbol{\theta}}^{ML} = \arg\max_{\boldsymbol{\theta}} P(\mathbf{Y}|\boldsymbol{\theta}). \tag{5}$$

Assume that $\boldsymbol{\epsilon} \sim \mathcal{WGN}(0, \mathbf{V}_{\boldsymbol{\epsilon}})$, that is, the measurement noise is white, zero-mean, and normally distributed with covariance matrix $\mathbf{V}_{\boldsymbol{\epsilon}}$. In particular, for independent noise acting on each output, the covariance matrix $\mathbf{V}_{\boldsymbol{\epsilon}}$ is diagonal with $\mathbf{V}_{\epsilon_{i,i}} = \sigma^2_{\epsilon_i}$. As typical in the literature, the measurement noise is assumed to be *independent, identically distributed*. Then the likelihood function can be expressed as [33]

$$P(\mathbf{Y}|\boldsymbol{\theta}) = \prod_{j=1}^{N_d} \frac{1}{\sqrt{2\pi^{N_y} \det(\mathbf{V}_{\boldsymbol{\epsilon}}^{-1})}} \exp\left(-\frac{1}{2}(\mathbf{y}_j - \hat{\mathbf{y}}_j(\boldsymbol{\theta}))^\top \mathbf{V}_{\boldsymbol{\epsilon}}^{-1}(\mathbf{y}_j - \hat{\mathbf{y}}_j(\boldsymbol{\theta}))\right) \tag{6}$$

where $\hat{\mathbf{y}}_j(\boldsymbol{\theta})$ is the model prediction for the jth experimental observation $\mathbf{y}_j$ based on the parameter $\boldsymbol{\theta}$, N_d is the number of available experimental data, N_y is the dimension of $\mathbf{Y}$, and superscript $\top$ is the matrix transpose.

Due to its monotonicity, a logarithmic transformation can be applied to compute the *log-likelihood*, which can be maximized in place of the standard likelihood function [33]:

$$\hat{\boldsymbol{\theta}}^{ML} = \arg\max_{\boldsymbol{\theta}} \ln(P(\mathbf{Y}|\boldsymbol{\theta})) \tag{7}$$

$$= \arg\min_{\boldsymbol{\theta}} -2\ln(P(\mathbf{Y}|\boldsymbol{\theta})) \tag{8}$$

$$= \arg\min_{\boldsymbol{\theta}} N_d \ln(2\pi^{N_y} \det(\mathbf{V}_{\boldsymbol{\epsilon}}^{-1})) + \sum_{j=1}^{N_d} \left((\mathbf{y}_j - \hat{\mathbf{y}}_j(\boldsymbol{\theta}))^\top \mathbf{V}_{\boldsymbol{\epsilon}}^{-1}(\mathbf{y}_j - \hat{\mathbf{y}}_j(\boldsymbol{\theta}))\right) \tag{9}$$

$$= \arg\min_{\boldsymbol{\theta}} \sum_{j=1}^{N_d} \left((\mathbf{y}_j - \hat{\mathbf{y}}_j(\boldsymbol{\theta}))^\top \mathbf{V}_{\boldsymbol{\epsilon}}^{-1}(\mathbf{y}_j - \hat{\mathbf{y}}_j(\boldsymbol{\theta}))\right) \tag{10}$$

$$=: \arg\min_{\boldsymbol{\theta}} J^{ML}(\boldsymbol{\theta}) \tag{11}$$

In this particular case, the maximum likelihood estimate coincides with *Least Squares* (LS), that is [33],

$$\hat{\boldsymbol{\theta}}^{LS} = \arg\min_{\boldsymbol{\theta}} \sum_{j=1}^{N_d} \left((\mathbf{y}_j - \hat{\mathbf{y}}_j(\boldsymbol{\theta}))^\top (\mathbf{y}_j - \hat{\mathbf{y}}_j(\boldsymbol{\theta}))\right). \tag{12}$$

2.3. Uncertainty analysis

The methodology discussed in Section 2.2 allows the determination of a parameter estimate based on experimental observations. Once a parameter estimate is available, it is advisable to quantify the uncertainty associated with the parameter estimate. This can be achieved by computing confidence regions for the parameter estimates, as discussed in this section.

2.3.1. Linearized sensitivity analysis and confidence regions

For a model that is linear in the parameters $\boldsymbol{\theta}$ with measurement noise that is normally distributed, the uncertainty affecting a parameter estimate (e.g., $\hat{\boldsymbol{\theta}}^{ML}$) can be characterized by computing a hyperellipsoid [33,35]. A widely used method for estimating the uncertainty in parameters in a nonlinear model is to replace the nonlinearity (1) by a first-order Taylor expansion, e.g.,

$$\hat{\mathbf{y}}_j(\boldsymbol{\theta}) \approx \hat{\mathbf{y}}_j(\hat{\boldsymbol{\theta}}^{ML}) + \mathbf{F}_j(\hat{\boldsymbol{\theta}}^{ML})(\boldsymbol{\theta} - \hat{\boldsymbol{\theta}}^{ML}) \tag{13}$$

where the sensitivity matrix is given by

$$\mathbf{F}_j(\hat{\boldsymbol{\theta}}^{ML}) = J_{\boldsymbol{\theta}}(\hat{\mathbf{y}}_j(\boldsymbol{\theta}))\Big|_{\boldsymbol{\theta}=\hat{\boldsymbol{\theta}}^{ML}} \tag{14}$$

where $J_{\boldsymbol{\theta}}$ refers to the Jacobian operator. The sensitivity matrix can be computed with finite differences, a forward sensitivity analysis, or an adjoint sensitivity analysis for all observed outputs and parameters.

The confidence region approximation Θ_α is then given by the hyperellipsoid [69]:

$$\Theta_\alpha = \left\{\boldsymbol{\theta} : \left(\boldsymbol{\theta} - \hat{\boldsymbol{\theta}}^{ML}\right)^\top \mathbf{V}_{\boldsymbol{\theta}}^{-1}\left(\boldsymbol{\theta} - \hat{\boldsymbol{\theta}}^{ML}\right) \le \chi^2_{N_p}(1-\alpha)\right\} \tag{15}$$

where $\chi^2_{N_p}$ is the chi-squared distribution with N_p degrees of freedom, N_p is the number of parameters, α is the level of significance, and the parameter covariance matrix is given by

$$\mathbf{V}_\theta^{-1} = \sum_{j=1}^{N_d} \mathbf{F}_j^\top \left(\hat{\theta}^{ML}\right) \mathbf{V}_\epsilon^{-1} \mathbf{F}_j \left(\hat{\theta}^{ML}\right) \tag{16}$$

Sensitivity analysis can also be used to reduce the dimension of the parameter space by establishing statistical significance with a sensitivity cutoff. The sensitivity of the chosen cost function (e.g., $J^{ML}(\theta)$) with respect to each candidate parameter is used to evaluate the impact of parameter variations. As discussed above, for models that are nonlinear in the parameters, the analysis can be based on its linearization around an interesting point of the parameter space [16,35,70,71].

2.3.2. Nonlinear confidence regions

While the above formulation is appropriate for linear or nearly linear systems, a linearized sensitivity analysis can produce misleading results for highly nonlinear systems, such as the electrochemical system investigated in this work. In order to provide a meaningful description of the uncertainty affecting parameter estimates, a more general approach should be applied. For the ML estimation introduced in Section 2.2 with normally distributed zero-mean noise, $J^{ML}(\theta)$ has a χ^2 distribution, i.e.,

$$\chi^2(\theta) = \sum_{j=1}^{N_d} \left((\mathbf{y}_j - \hat{\mathbf{y}}_j(\theta))^\top \mathbf{V}_\epsilon^{-1} (\mathbf{y}_j - \hat{\mathbf{y}}_j(\theta))\right) = J^{ML}(\theta). \tag{17}$$

The nonlinear confidence region Θ_α is described by all θ that satisfy the inequality

$$\Theta_\alpha = \left\{ \theta : \chi^2(\theta) - \chi^2\left(\hat{\theta}^{ML}\right) \leq \chi^2_{N_p}(1-\alpha) \right\}, \tag{18}$$

and can be mapped by evaluating $\chi^2(\theta)$ over a grid of values in the parameter space.

For nonlinear models, the shape of Θ_α may not be ellipsoidal and strongly depends on the significance level α. To obtain a quantitative understanding of the shape, the procedure can be repeated for different values of α, e.g., 0.01, 0.05, 0.1, which correspond to 99%, 95% and 90% confidence regions, respectively. In contrast, the linearization approach produces an ellipsoidal confidence region that can be highly inaccurate and misleading for the purpose of identifiability analyses. Any approach for the accurate computation of Θ_α for a nonlinear model comes at the price of a higher computational complexity. Specifically, a high number of model evaluations may be required if the parameter space is large. Such function evaluations are independent on each other, however, and can be easily performed in parallel to reduce computational cost.

2.4. Identifiability analysis

Before carrying out parameter identification for a complex, nonlinear model, a parameter identifiability analysis should be performed to determine whether the model structure, noise level, and operating regime allow the parameters to be estimatable from the available experimental data. In particular, a parameter is said to be *identifiable* if *univocally* estimable from the experimental data. When not identifiable, the parameter is said to be *unidentifiable*. Parameter *unidentifiability* can be classified based on its origin: *structural unidentifiability* in which parameter groupings in the set of modeling equations cannot be solved uniquely, and *practical unidentifiability* in which regression to experimental data leads to non-unique results [35]. While structural unidentifiability is strictly related to the choice of the model structure, practical unidentifiability depends on both model structure and informativity of the available dataset.

Practical identifiability of a parameter can be assessed by verifying that its confidence region is finitely bounded. If not, the parameter is practically unidentifiable, and an unbounded set of parameter values can describe the experimental data within desired level of confidence. The techniques in Sections 2.3.1 and 2.3.2 allow the computation of linear and nonlinear confidence regions, and can be exploited to study parameter identifiability. When investigating parameter identifiability for a nonlinear model, the linearized approach in Section 2.3.1 may not be suitable, as the resulting confidence region can be highly inaccurate and misleading.

As an example, consider a nonlinear model with $\theta \in \mathbb{R}^2$. Two-dimensional contour plots of $\chi^2(\theta) - \chi^2(\theta^*)$, and the nonlinear confidence regions Θ_α in Figs. 2 illustrate four distinct cases:

- The confidence region is finitely bounded, i.e., both parameters θ_1 and θ_2 are identifiable (Fig. 2(a)). A linearized analysis would produce reasonable results, and the χ^2 function is strictly convex and characterized by a unique optimizer.
- The parameter θ_1 is identifiable and the parameter θ_2 is unidentifiable (Fig. 2(b)). The confidence region is bounded only in the θ_1 direction. The χ^2 function is not convex and admits infinitely many minima. The confidence region obtained by linearization at any point along the chi-squared minimum is inaccurate (either has an upper and lower bound on θ_2, or has no bounds on θ_2). Moreover, numerical optimization may produce very different results, depending on the initial guess for the parameter.
- Both parameters are globally unidentifiable, as the confidence region is unbounded on both sides (Fig. 2(c)). As in the previous case, the χ^2 function is non-convex, and admits infinitely many minima that lie within the bounds of the confidence region. Specifically, the confidence region assumes a banana-like shape. This scenario is particularly critical if a linearized analysis is carried out, since the resulting sensitivities are heavily dependent on the linearization point. For example, linearization around point A would result in strong sensitivity along the θ_1 direction, but a very low sensitivity in the θ_2 direction. In contrast, linearization around point B would result in strong sensitivity along the θ_2 direction, but a very low sensitivity in the θ_1 direction. For both linearization points, the parameters would appear as being locally identifiable. Moreover, numerical optimization at any initial guess would converge to a point on the minimum curve that would locally appear to be minimum over θ_1 for fixed θ_2 and locally appear to be minimum over θ_2 for fixed θ_1.
- Both parameters are unidentifiable (Fig. 2(d)). The confidence region is unbounded on both sides, and the χ^2 function admits infinitely many minima.

2.5. Identifiability methodology

In this work, a local identifiability analysis is performed for synthetic data generated by an MPET model of A123 System's *APR18650M1A* Lithium Iron Phosphate (LFP) batteries [72]. Specific details of the MPET modeling are given in Section 3.1. The synthetic data includes Gaussian distributed measurement noise, with zero mean and known standard deviation. In this way, both θ^* and σ_ϵ are known. Knowing the "ground truth" used to construct the data enables insights to be gained into potential biases occurring during parameter estimation, which would be less evident if the methodology was directly applied to experimental data (i.e., without knowledge of θ^* and σ_ϵ). The parameter estimation is based on the ML approach summarized in Section 2.2, and is performed on a logarithmic basis of θ. This is a standard approach used to improve numerical convergence for parameters that can change by many orders of magnitude [35].

The identifiability analysis consists of four steps:

1. A *linearized sensitivity analysis* is performed around θ^* to give a preliminary evaluation of the impact of each parameter variation on the battery output voltage, which is used as dependent variable for parameter estimation. This approach is commonly

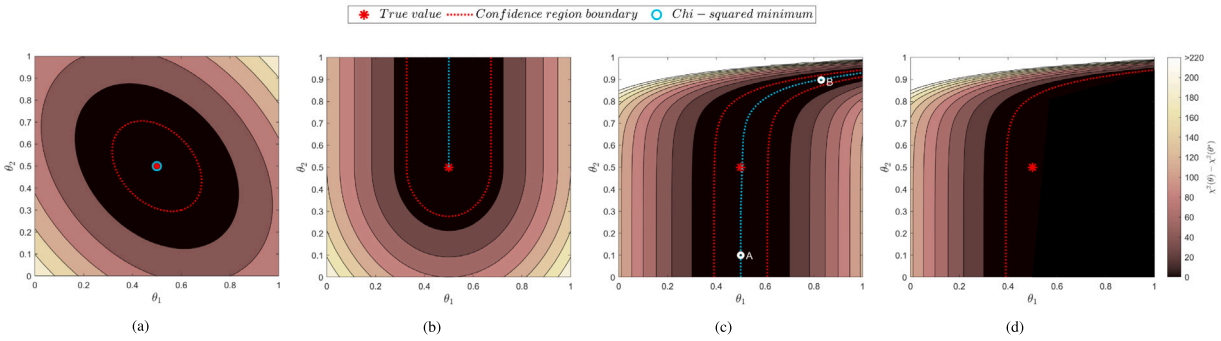

Fig. 2. Example chi-squared distributions for (a) a pair of identifiable parameters, (b) one unidentifiable and one identifiable parameters, (c) a pair of globally unidentifiable parameters that are locally identifiable, and (d) a pair of simultaneously unidentifiable parameters. The chi-squared minimum is the manifold of parameter values that minimize the chi-squared function.

applied in the Li-ion battery literature [22,24,73], and works as a baseline identifiability analysis. Sensivity is quantified by the *Cumulative Absolute Sensitivity* (CAS),

$$\mathrm{CAS}_k = \sum_{j=1}^{N_d} |\mathbf{F}_{j,k}|, \tag{19}$$

where $\mathbf{F}_{j,k}$ is the kth element of the sensitivity matrix of the jth experimental observation $\mathbf{F}_j$. The sensitivities are computed via central finite difference approximation, relying on three different differentiation step sizes for sake of comparison. Moreover, a local uncertainty quantification is performed, based on results derived from the linearized sensitivity.

2. A *two-dimensional nonlinear confidence region mapping* is performed for all possible combinations of two parameters. Parameters not belonging to the couple under investigation are set to their true values. This thorough mapping allows to provide further insight and classify couples of parameters according to the taxonomy discussed with Fig. 2.
3. A *three-dimensional nonlinear confidence region mapping* is performed for all possible combinations of three parameters. Parameters not belonging to the triplet under investigation are set to their true values. Due to the high number of parameters, this step only focuses on those parameters which always resulted in identifiable couples, based the previous step of the analysis. This further step of the analysis allows to study parameter identifiability when triplets of parameters are identified at the same time.

Remark. The analysis based on two- or three-dimensional nonlinear confidence region mapping facilitates investigation of *local* identifiability issues, respectively. This approach produces highly detailed visualizations of the shape of the confidence regions, which are not provided when applying tools for *global* analysis, such as MCMC methods, to systems with more than three parameters [31].

2.6. Interpreting identifiability

Broadly speaking, a parameter is said to be *practically unidentifiable* if the same model output is generated for different values of the parameter. From a physical perspective, this may occur if e.g., the part of the battery dynamics controlled by the parameter under investigation is limited by other factors. As an example, in case of reaction-limited dynamics, parameters related to diffusion may be practically unidentifiable, while, in the opposite case of diffusion-limited dynamics, parameters related to reaction may be practically unidentifiable. Another possible situation leading to practical unidentifiability involves parameters simultaneously affecting the model output in the same way. In this scenario, it is not possible to correctly separate the effect of each of the parameters on the model output. This effect can be demonstrated by the "resistances in series" case study, analyzed and discussed in detail in [31].

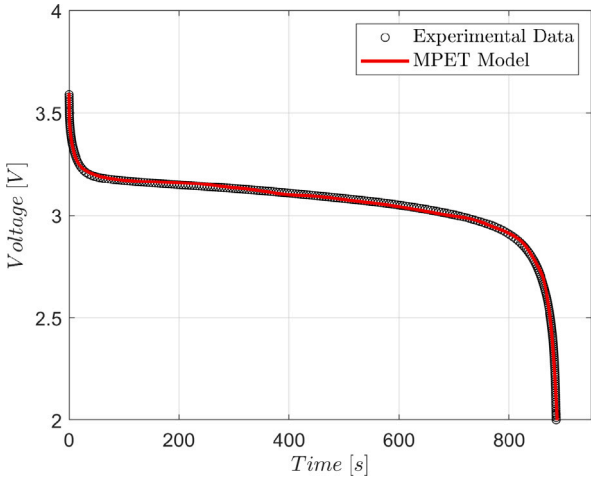

Fig. 3. Comparison of experimental data and MPET-predicted discharge curve at a C-rate of 4C.

Table 1
Nominal parameter values (θ_i^*), lower bounds ($\theta_{lb,i}$), and upper bounds ($\theta_{ub,i}$) adopted for parameter estimation and identifiability analysis.

Parameter	$\ln \theta_i^*$	$\ln \theta_{lb,i}$	$\ln \theta_{ub,i}$
Ω_a^a	−20.4765	−21.7775	−19.1755
Ω_b^a	−20.0393	−21.3403	−18.7382
κ^a	−6.39794	−7.69897	−5.09691
D^a	−11.9031	−20.301	−9.69897
k_0^a	2.09325	−0.30103	3.30103
R_{film}^a	−2.01812	−5.30103	−1.69897
Ω_a^c	−19.7314	−21.0325	−18.4304
κ^c	−9.29975	−10.6008	−7.99872
B^c	8.2824	6.98137	9.58343
D^c	−18.2757	−20.301	−9.69897
k_0^c	−0.533281	−2.30103	2.30103
R_{film}^c	−2.0019	−5.30103	−1.69897
D_+^e	−9.46884	−11.301	−7.69897
D_-^e	−8.53187	−11.301	−7.69897

3. Results

This section applies the methodology in the previous section to a specific case study.

3.1. Case study

This work examines the parameter identifiability of an MPET model of A123 System's *APR18650M1A* LFP batteries [72]. The cells are characterized by a nominal capacity of 1.1 A/h, and a charge cutoff

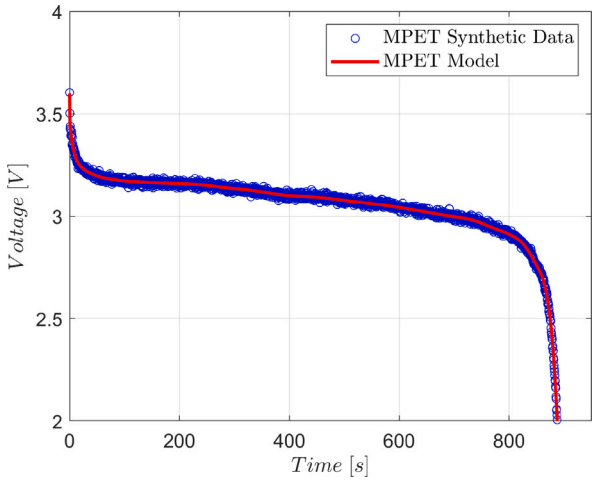

Fig. 4. Comparison of MPET-generated, nominal and noise-corrupted discharge curves at a C-rate of 4C.

voltage of 3.6 V. Further details of the case study can be found in [17]. Details regarding the corresponding MPET model are given in the reminder of this section. A schematic of the MPET model is shown in Fig. 1.

Anode, cathode and separator thicknesses are set to 38, 79, and 25 μm, respectively. Volume loading percents of active material for anode and cathode are 0.9 and 0.84, respectively. The anode, cathode and separator have porosities of 0.377, 0.421, and 0.304, respectively, and the associated Bruggeman exponents are −1.341, −1.8125, and −2.3435. The anode and cathode have a bulk conductivity of 0.04 S and 2.077 S.

Anode, cathode, and separator are discretized in 10 volumes, and 10 representative particles are used for each volume. Graphite particles in the anode are modeled as cylindrical, with radii drawn from a lognormal distribution with mean of 273 nm and standard deviation of 10.73 μm. The cylinder height is set to 20 nm; a Cahn–Hilliard Reaction model [61] is assumed for the anode particles [36,56,57]. Moreover, anode particles are characterized by a conductance value drawn from a lognormal distribution, with mean of 114.7 nS and standard deviation of 0.1 nS. Particles in the cathode are modeled as rectangular (approximating platelet in shape), with thickness of 20 nm and main dimension drawn from a lognormal distribution with mean and standard deviation of 11.01 and 10.13 nm; an Allen–Cahn Reaction model [61] is assumed for the cathode particles [36,50–53]. Moreover, cathode particles are characterized by a conductance value drawn from a lognormal distribution, with mean of 9.23 nS and standard deviation of 0.1 nS. Butler–Volmer kinetics with an associate film resistance is considered for both electrodes. The functional forms defining the chemical potential of anode and cathode active materials (LiC_6 and $LiFePO_4$) are reported in Appendix. The electrolyte follows a dilute solution model, with an initial concentration of 1.077 kmol/m^3. The values of parameters subject to identifiability analysis are reported in Table 1. The MPET model parameters were obtained by combining values from the literature and results of a parameter estimation procedure based on experimental charge and discharge curves in the range [1, 10]C. The parameters were selected to closely fit a specific 4C discharge curve from [17], as depicted in Fig. 3. This last step ensures the existence of a set of parameters that closely fit real experimental data, and allows to study identifiability in absence of model bias. Then, a 4C discharge is simulated with the MPET model, and corrupted with zero mean, white measurement noise, characterized by a standard deviation of $\sigma_\epsilon = 10$ mV. Fig. 4 depicts both the original and the noise-corrupted discharge curves. In this work, the parameter identifiability analysis is based on a set of 364 samples from the noise-corrupted 4C discharge curve.

Table 2
Cumulative absolute sensitivities of voltage V to parameter variations of 0.1%, 0.5%, and 1% of the logarithm of the nominal parameter values $\ln \theta_i^*$.

	Cumulative absolute sensitivity		
Parameter	0.1%	0.5%	1%
Ω_a^a	7.3311	7.4186	7.7352
Ω_b^a	154.7781	155.4275	157.664
κ^a	0.044269	0.014853	0.011143
D^a	0.93224	0.93628	0.9466
k_0^a	15.6501	15.7321	15.7675
R_{film}^a	147.3171	147.255	147.3863
Ω_a^c	376.7667	373.6268	392.181
κ^c	1.8067	1.809	1.8197
B^c	0.36738	0.37295	0.41549
D^c	0	0	0
k_0^c	14.0113	14.2264	14.1967
R_{film}^c	1.2465	1.143	1.1449
D_+^e	373.9655	376.8729	397.9823
D_-^e	0.89063	0.89653	0.90167

The analysis focuses on a set of 14 parameters, whose true value θ^* is reported in Table 1. The parameters pertaining to the anode are the regular solution parameters Ω_a^a [J] and Ω_b^a [J], the interfacial gradient penalty κ^a [J/m], the Li solid transport coefficient D^a [m^2/s], the BV reaction rate k_0^a [A/m^2], and the BV film resistance R_{film}^a [mΩ/m^2]. For the cathode, the associated parameters are the regular solution parameters Ω_a^c [J], the interfacial gradient penalty κ^c [J/m], the stress coefficient B^c [Pa], the Li solid transport coefficient D^c [m^2/s], the BV reaction rate k_0^c [A/m^2], and the BV film resistance R_{film}^c [mΩ/m^2]. For the dilute electrolyte, the two transport coefficients D_+^e [m^2/s] and D_-^e [m^2/s] are considered. Table 1 reports the intervals of the parameter values considered as being physically meaningful in this work.

The analysis is performed for the logarithm of the parameters θ, which is a standard approach in parameter estimation procedures to improve numerical convergence for parameters that can vary by many orders of magnitude.

3.2. Linearized sensitivity analysis

We first consider a linearized sensitivity analysis performed around the true parameter values θ^*. Sensitivities are computed by the central finite difference method, relying on three different step sizes (0.1%, 0.5%, and 1% of the nominal parameter value) for sake of comparison. Results are quantified in term of CAS, as defined in (19), and reported in Table 2. To ease comparison and ranking of CAS values, Fig. 5 depicts *normalized* CAS values (rescaled between 0 and 1) for each finite difference differentiation step size. The analysis of sensitivities, both in terms of absolute and normalized CAS, indicate that the three step sizes produce consistent results. In particular, the cathode regular solution parameter Ω_a^c and the electrolyte diffusivity coefficient D_+^e are associated with the highest CAS values, followed by the anode regular solution parameter Ω_b^a and anode film resistance R_{film}^a, which exhibit about 40% of the maximum CAS. The two reaction rates, k_0^a and k_0^c, follow in the ranking with about 5% of the maximum CAS. About 2% of the maximum CAS is associated with the anode regular solution parameter Ω_a^a. All other parameters are associated with lower sensitivity values. In particular, the parameter sensitivity for the cathode solid transport coefficient D^c is zero. Variations of this parameter in a neighborhood of the nominal value does not affect the measured output voltage for the specific experimental design.

3.3. Linearized identifiability analysis

One way to estimate the uncertainty associated with the parameter estimates employs the linearized sensitivities, as discussed in Section 2.3.1. In particular, (16) allows computing the parameter estimate *precision matrix* $\mathbf{V}_\theta^{-1}$, the inverse of the parameter covariance

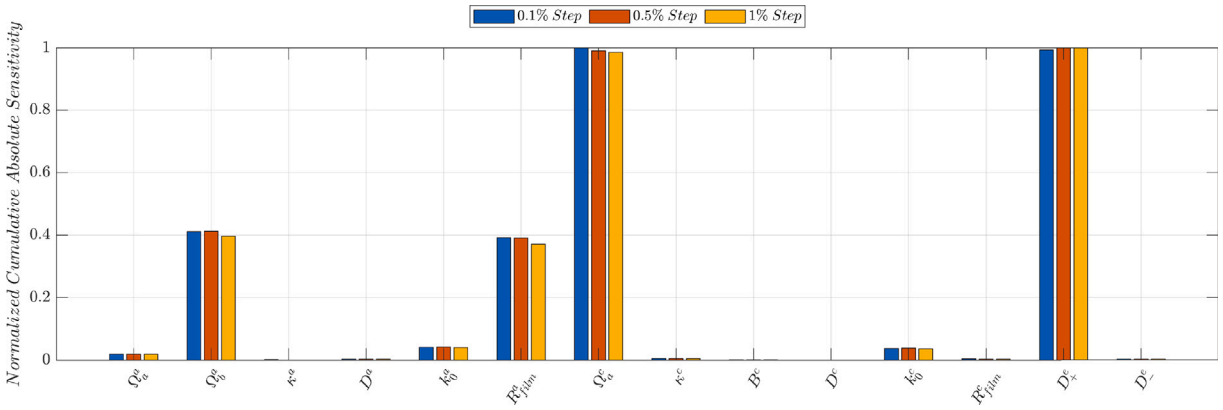

Fig. 5. Normalized cumulative absolute sensitivities of voltage V to parameter variations of 0.1% (blue bar), 0.5% (orange bar), and 1% (yellow bar) of the logarithm of the nominal parameter value θ^*. (For interpretation of the references to color in this figure legend, the reader is referred to the web version of this article.)

Table 3
Standard deviations of the logarithm of the parameter estimates θ_i for the reduced parameter set (D^c excluded from the original set).

		σ_θ		
Parameter	$\ln \theta_i^*$	0.1%	0.5%	1%
Ω_a^a	−20.4765	0.32081	0.33129	0.31307
Ω_b^a	−20.0393	0.12389	0.12969	0.10558
κ^a	−6.3979	2.1751	4.311	4.8909
D^a	−11.9031	0.99492	0.98197	0.97152
k_0^a	2.0932	0.21754	0.2137	0.21462
R_{film}^a	−2.0181	0.078945	0.074576	0.070038
Ω_a^c	−19.7314	0.10134	0.10317	0.08932
κ^c	−9.2997	0.85785	0.83467	0.82232
B^c	8.2824	1.3795	1.2836	1.0626
k_0^c	−0.53328	0.25663	0.26287	0.23977
R_{film}^c	−2.0019	0.90989	1.0055	0.87714
D_+^e	−9.4688	0.087459	0.080101	0.076816
D_-^e	−8.5319	0.41912	0.41728	0.42227

matrix. Due to the zero sensitivity of voltage to the cathode stress coefficient B^c, $\mathbf{V}_{\boldsymbol{\theta}}^{-1}$ has a zero row and column corresponding to this parameter, and the *identifiability condition* for the linearized model ($\text{rank}(\sum_{j=1}^{N_d} \mathbf{F}_j^\top \mathbf{F}_j) = \min\{N_d, N_p\}$) is not fulfilled. Consequently, the minimum of the (linearized) ML cost function is not unique, and lies on a manifold of the parameter space, aligned with the D^c direction. Such a parameter can be excluded from a parameter estimation procedure by, for example, fixing its value to a constant from the literature. Moreover, when possible, a more informative experimental design may be sought, to improve parameter identifiability properties.

Consider now a reduced parameter set, obtained by the cathode stress coefficient D^c from the original set. Based on the sensitivities, it is now possible to compute the parameter covariance matrix $\mathbf{V}_{\boldsymbol{\theta}}$. Table 3 summarizes the standard deviation associated with each parameter in the reduced set, for the three finite difference steps. In this case, all the standard deviations have finite values. As expected from the analysis of sensitivities, some parameters are associated to high standard deviations. Specifically, the standard deviations for κ^a, k_0^c, B^c, R_{film}^c, are the same order of magnitude of the true parameter value; for other parameters, the standard deviations assume values which are typically one or two order of magnitude smaller than the corresponding true parameter value.

3.4. Nonlinear confidence regions

While the linearized analysis performed in the previous section is a common approach in the literature, its results can be misleading for a highly nonlinear system such as a lithium-ion battery. When possible, a more detailed analysis based on the full nonlinear model is advised. As discussed in 2.3.2, nonlinear confidence regions can be visually inspected by explicitly computing the chi-squared difference $\chi^2(\boldsymbol{\theta}) - \chi^2(\hat{\boldsymbol{\theta}}^{ML})$ over a sufficiently fine grid in the parameter space, and plotting the results as contour plots. While this analysis can be performed in two or three dimensions only, it provides an extremely detailed knowledge of the confidence regions and, in turn, is able to provide detailed insight about local identifiability properties of couples/triplets of parameters. In the subsequent analysis, $\chi^2(\hat{\boldsymbol{\theta}}^{ML})$ is taken as the chi-squared minimum *over the considered grid* in the parameter space.

3.4.1. 2D nonlinear confidence regions

The analysis starts by considering all possible combinations of two parameters. Parameters not belonging to the couple were set to their true values. For each combination, the chi-squared difference is computed over the parameter space defined by bounds reported in Table 1. The chi-squared limit value, defining the boundary of confidence regions, is given by $\chi_2^2(0.95) = 5.99$. Fig. 6 depicts examples of 2D chi-squared difference plots and confidence regions. Inspection of such plots allows the classification of couples of parameters in terms of local identifiability in a neighborhood of the true parameter values. Table 4 summarizes the classification. The analysis of Table 4 highlights that a group of parameters always appears as locally identifiable, regardless of the other parameter in the couple:

$$\boldsymbol{\Theta}_{\boldsymbol{2D}}^{\boldsymbol{I}} = \{\Omega_a^a,\ \Omega_b^a,\ k_0^a,\ R_{\text{film}}^a,\ \Omega_a^c,\ k_0^c,\ D_+^e\}. \tag{20}$$

The cathode interfacial gradient penalty, κ^c, only appears as locally unidentifiable in combination with the anode solid transport coefficient D^a, while being locally identifiable in all other combinations. A group of parameters always appears as locally unidentifiable, regardless of the other parameter in the couple:

$$\boldsymbol{\Theta}_{\boldsymbol{2D}}^{\boldsymbol{U}} = \{k^a,\ B^c,\ D^c,\ R_{\text{film}}^c,\ D_-^e\}. \tag{21}$$

Finally, the anode solid transport coefficient D^a is locally identifiable only in combination with the cathode film resistance R_{film}^c or the electrolyte diffusivity coefficient D_+^e, while being locally unidentifiable in all other cases. A comparison with the results of the linearized sensitivity analysis highlights that all the parameters associated to high sensitivity values now appear in $\boldsymbol{\Theta}_{\boldsymbol{2D}}^{\boldsymbol{I}}$, while parameters associated with lower values appear in $\boldsymbol{\Theta}_{\boldsymbol{2D}}^{\boldsymbol{U}}$. The unidentifiability of the cathode solid transport coefficient D^c, which is characterized by zero linearized sensitivity, is confirmed by this nonlinear analysis. As an example, Fig. 6(c) shows the chi-squared difference plot for a couple of parameters including D^c. The chi-squared minimum lies on a line in the D^c direction, as expected from the linearized analysis.

For the majority of parameters, the results of the 2D nonlinear analysis are aligned with those from the linearized sensitivity and

Table 4
Results of nonlinear identifiability analysis with 2D contour plots. The following notation is used for each table entry (row,column): I = Identifiable parameter (green); U = Unidentifiable parameter (red).

Parameter	Ω_a^a	Ω_b^a	κ^a	D^a	k_0^a	R_{film}^a	Ω_a^c	κ^c	B^c	D^c	k_0^c	R_{film}^c	D_+^e	D_-^e
Ω_a^a	–	I,I	I,U	I,U	I,I	I,I	I,I	I,I	I,U	I,U	I,I	I,U	I,I	I,U
Ω_b^a	I,I	–	I,U	I,U	I,I	I,I	I,I	I,I	I,U	I,U	I,I	I,U	I,I	I,U
κ^a	U,I	U,I	–	U,U	U,I	U,I	U,I	U,I	U,U	U,U	U,I	U,U	U,I	U,U
D^a	U,I	U,I	U,U	–	U,I	U,I	U,I	U,U	U,U	U,U	U,I	I,U	I,I	U,U
k_0^a	I,I	I,I	I,U	I,U	–	I,I	I,I	I,I	I,U	I,U	I,I	I,U	I,I	I,U
R_{film}^a	I,I	I,I	I,U	I,U	I,I	–	I,I	I,I	I,U	I,U	I,I	I,U	I,I	I,U
Ω_a^c	I,I	I,I	I,U	I,U	I,I	I,I	–	I,I	I,U	I,U	I,I	I,U	I,I	I,U
κ^c	I,I	I,I	I,U	U,U	I,I	I,I	I,I	–	I,U	I,U	I,I	I,U	I,I	I,U
B^c	U,I	U,I	U,U	U,U	U,I	U,I	U,I	U,I	–	U,U	U,I	U,U	U,I	U,U
D^c	U,I	U,I	U,U	U,U	U,I	U,I	U,I	U,I	U,U	–	U,I	U,U	U,I	U,U
k_0^c	I,I	I,I	I,U	I,U	I,I	I,I	I,I	I,I	I,U	I,U	–	I,U	I,I	I,U
R_{film}^c	U,I	U,I	U,U	U,I	U,I	U,I	U,I	U,I	U,U	U,U	U,I	–	U,I	U,U
D_+^e	I,I	I,I	I,U	I,I	I,I	I,I	I,I	I,I	I,U	I,U	I,I	I,U	–	I,U
D_-^e	U,I	U,I	U,U	U,U	U,I	U,I	U,I	U,I	U,U	U,U	U,I	U,U	U,I	–

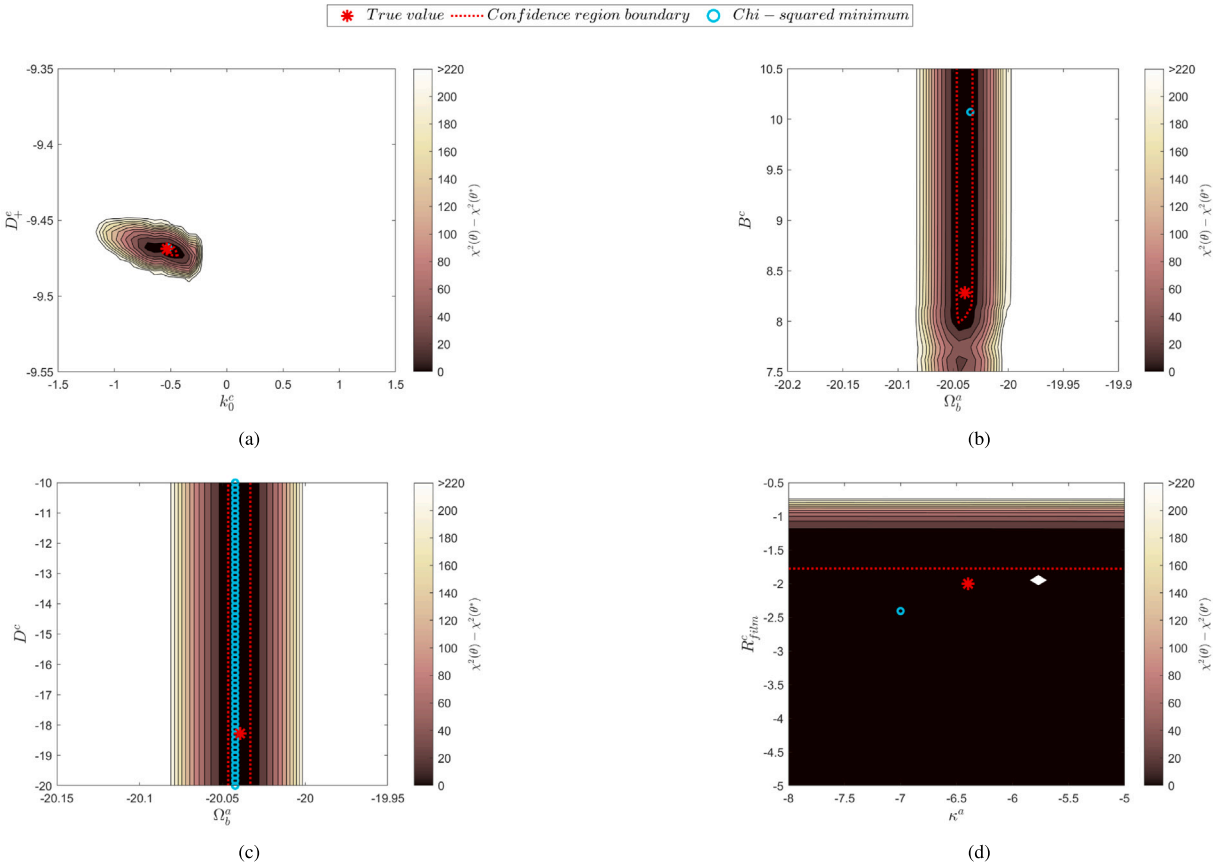

Fig. 6. Local confidence regions for sets of two parameters in θ, where the parameters excluded from each plot are set to their true value. The chi-squared limit value, defining the boundary of the confidence regions, is given by $\chi_2^2(0.95) = 5.99$. The results are presented in terms of the logarithmic of each parameter in θ.

identifiability analyses. Parameters associated with rather low uncertainty (high sensitivity) by the linearized analysis appear as locally identifiable also with the two-dimensional nonlinear analysis, and vice versa, with few exceptions. Specifically, the cathode reaction rate k_0^c, whose standard deviation from the linearized analysis is rather high, appears as locally identifiable in the 2D nonlinear analysis. In contrast, the electrolyte diffusivity coefficient D_-^e is associated with a reasonable standard deviation for the linearized analysis, but appears as locally unidentifiable in the 2D nonlinear analysis. It is also interesting to note that, for the finitely bounded, two-dimensional nonlinear regions in Fig. 6(c)a, the shape of the region can be reasonably approximated by an ellipsoid.[1]

3.4.2. 3D nonlinear confidence regions

This section constructs nonlinear confidence regions for triplets of parameters. Due to the high number of possible combinations, the

[1] Local confidence regions obtained by nonlinear analysis are not necessarily ellipsoids in general.

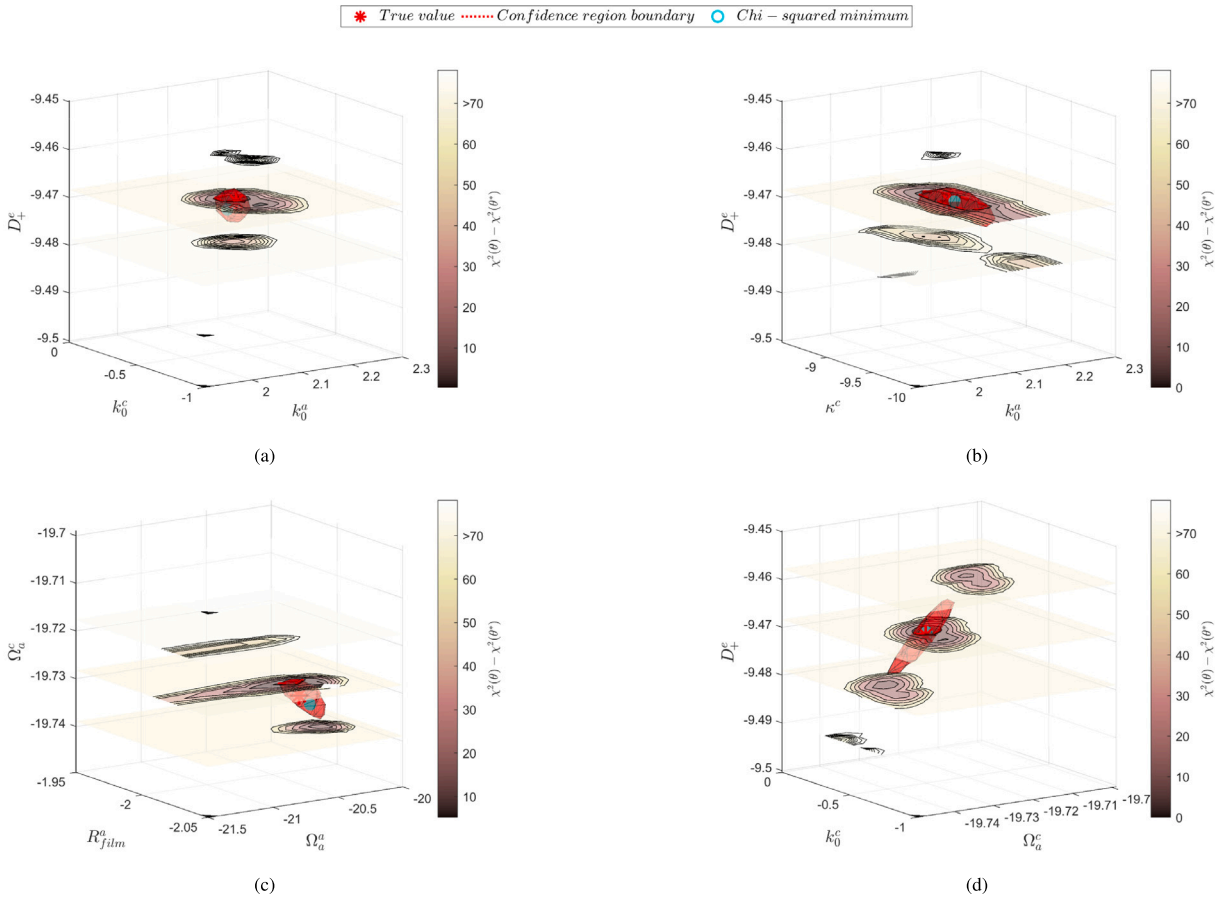

Fig. 7. Local confidence regions for sets of three parameters in θ, where the parameters excluded from each plot are set to their true value. The chi-squared limit value, defining the boundary of the confidence regions, is given by $\chi^2_3(0.95) = 7.82$. The results are presented for the logarithm of each parameter in θ.

Table 5
Results of nonlinear identifiability analysis with 3D contour plots. The following notation is used for each table entry (row,column): I=Identifiable parameter (green); U=Unidentifiable parameter (red).

Parameter triplet	Identifiability
$(\Omega_a^a, \kappa^c, k_0^c)$	(I,U,I)
$(\Omega_a^c, \kappa^c, k_0^c)$	(I,U,I)
(κ^c, k_0^c, D_+^e)	(U,I,I)

analysis focuses on the parameters belonging to $\boldsymbol{\Theta}^{\boldsymbol{I}}_{\boldsymbol{2D}}$, as well as on the cathode interfacial gradient penalty, κ^c, with the aim of verifying their local identifiability in a higher dimensional setting. Parameters not belonging to the triplet under investigation were set to their true values. Again, the chi-squared difference is computed over a three-dimensional grid in the parameter space, and confidence regions are computed based on the chi-squared limiting value $\chi^2_3(0.95) = 7.82$. Fig. 7 plots 3D confidence regions. For the majority of combinations, all parameters are locally identifiable. As in the two-dimensional case, when the three-dimensional nonlinear confidence regions are bounded, their shape are reasonably approximated by a hyperellipsoid. On the other hand, three parameter combinations result in one parameter being locally non-identifiable, as reported in Table 5 and depicted in Fig. 8. Specifically, the cathode interfacial gradient penalty, κ^c, shows identifiability issues when estimated in combination with regular solution parameters Ω_a^a or Ω_a^c, cathode reaction rate k_0^c, or electrolyte diffusivity coefficient D_+^e. It is interesting that, in all three combinations, the confidence region is composed of a bounded, nearly ellipsoidal-shaped component, and another tube-shaped, unbounded component, which is completely detached from the former. In this scenario, the interfacial gradient penalty κ^c is locally identifiable for some values of the other two parameters in the triplet, while being locally unidentifiable for other values. Again, this stresses the importance of a full nonlinear analysis of practical identifiability. To sum up, the 3D analysis confirms local identifiability for all parameters already local identifiable in 2D, and highlights further cases of local unidentifiability for the cathode interfacial gradient penalty κ^c:

$$\boldsymbol{\Theta}^{\boldsymbol{I}}_{\boldsymbol{3D}} = \{\Omega_a^a,\ \Omega_b^a,\ k_0^a,\ R^a_{\text{film}},\ \Omega_a^c,\ k_0^c,\ D_+^e\}. \tag{22}$$

4. Discussion

Several works in the PET literature [20,29,31] show that the kinetic and transport parameters are not fully identifiable when only using data from discharge curves under standard operations. For instance, discharge data for a reaction-limited cell cannot yield identifiable diffusion parameters. Similar considerations can be drawn for MPET models, whose parameter identifiability is investigated for the first time in this work. Even in a neighborhood of the true value, some of these parameters are unidentifiable at the 4C discharge rate analyzed in this work. In this case, identifiability could be improved by gathering data at C-rates $\ll$ 1C, which better approximates the open-circuit voltage and probes the equilibrium materials properties rather than transport properties. Identifiability could presumably be further improved by including additional transient data, such as the nonlinear response to voltage or current pulses, charging data, and data collected at a variety of different temperatures and C-rates [67,68]. On the other hand, the identifiability analysis also suggests that a group of parameters is locally identifiable, regardless of the other parameters on the couple/triplet. These parameters are

$$\boldsymbol{\Theta}^{\boldsymbol{I}} = \{\Omega_a^a,\ \Omega_b^a,\ k_0^a,\ R^a_{\text{film}},\ \Omega_a^c,\ k_0^c,\ D_+^e\}. \tag{23}$$

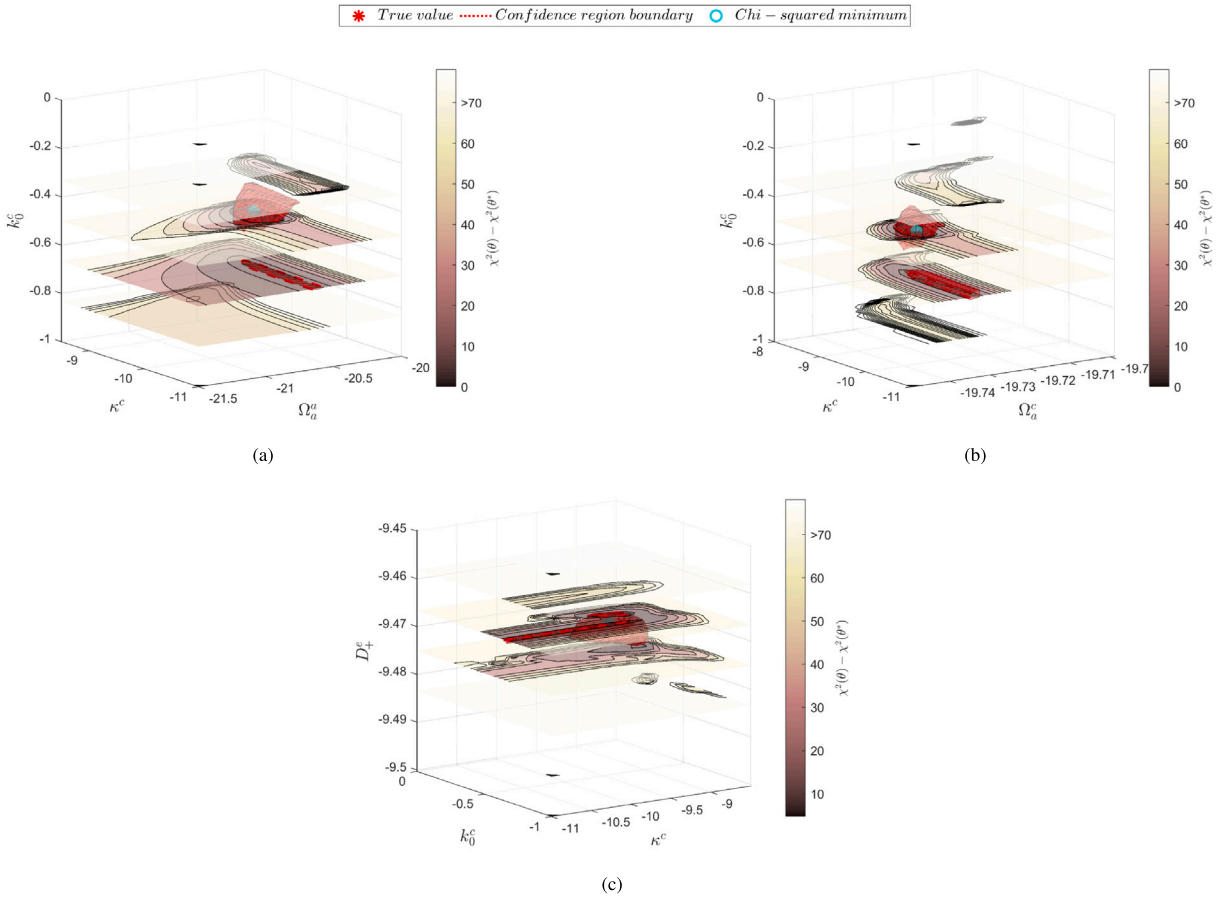

Fig. 8. Local confidence regions for sets of three parameters in θ, where the parameters excluded from each plot are set to their true value. The chi-squared limit value, defining boundary of confidence regions, is given by $\chi^2_3(0.95) = 7.82$. The results are presented for the logarithm of each parameter in θ.

It is interesting that all three regular solution parameters Ω^a_a, Ω^a_b, and Ω^c_a are identifiable, whereas the other parameters defining the free energy and chemical potential of active materials may not be identifiable with the available dataset. Physically, the regular solution parameters Ω^a_a, Ω^a_b, and Ω^c_a control phase separation in the active materials, so their robust identifiability underscores the importance of correctly modeling multiphase thermodynamics in MPET (which is neglected in PET). This result is also aligned with the preliminary findings discussed in [19], which highlighted possible lack of identifiability for the group of chemical potential parameters. That preliminary analysis was carried out considering a single particle per volume, and discharge currents in the range [0.1;4]C. The identifiability of the reaction kinetics parameters (k^c_0, k^a_0, R^a_{film}) and non-identifiability of the solid diffusivities (D^a, D^c) for both electrodes supports the hypothesis that multi-phase active materials in Li-ion batteries tend to be reaction-limited [38,49,50,54,58–60], until electrolyte diffusion becomes rate-limiting in porous electrodes at high currents [36,37], as further indicated by the identifiability of the electrolyte Li+ diffusivity D^e_+. It is also important to highlight that, while this work mainly focuses on a detailed local analysis of parameter confidence regions, it would be interesting to extend the results by assessing global practical identifiability properties of the parameter set. This goal could be achieved with the application of an MCMC approach [31]. The combination of global results from MCMC and local results from the nonlinear confidence region mapping would give a complete overview of parameter identifiability issues for the considered MPET model.

4.1. Removing practical unidentifiability

As discussed in this article, identifiability analyses can highlight that some parameter cannot be unequivocally identified from the available experimental data. Moreover, the visual analysis of the chi-squared function suggests that, in presence of practically unidentifiable parameters, the optimization algorithms adopted for parameter estimation may not converge to the neighborhood of the true parameter value. While it is well-known that local minima often arise in nonlinear models, the presence of wide, nearly flat areas of the chi-squared function may even result in failure of the optimization algorithm to converge to any point in the parameter space. For these reasons, the knowledge of possible identifiability issues can greatly ease the task of parameter estimation. Specifically, practically unidentifiable parameters can be dealt with by

1. setting such parameters to constant values;
2. using informative priors in the parameter estimation setup (MAP estimation);
3. applying model reduction;
4. collecting more informative data.

Fixing parameters to constant values is the simplest way to remove identifiability problems. Unidentifiable parameter values can be set according to the literature, estimated from computational chemistry calculations, or estimated with a separate parameter estimation procedure and an ad-hoc experimental dataset. The choice of fixing unidentifiable parameters to constant values also reduces the degrees of freedom of the parameter estimation problem, as well as the computational complexity of the associated optimization. Care must be taken to choose parameter values that fall within the parameter confidence

regions. While such choices are straightforward for globally unidentifiable parameters due to unboundedness of the confidence regions, for locally unidentifiable parameters, the detailed knowledge of such regions is required to avoid issues. The methodology discussed in this work for the computation of nonlinear confidence regions is therefore particularly important for this task. Moreover, when dealing with practical identifiability problems, fixing parameter values to constant values may deteriorate the fitting performance of the overall model. Finally, estimates for parameters may widely vary from source to source: this approach unavoidably introduces arbitrariness in the overall parameter estimation procedure.

The use of a MAP estimation methodology with informative priors can greatly reduce identifiability problems, while avoiding the issues caused by fixing the values of parameters to constants. MAP estimation explicitly accounts for the level of uncertainties in the prior estimates of the parameters and allows for more flexibility in the parameter estimation optimization compared to the above procedure of setting unidentifiable parameters to constants. As an example, consider the MAP approach introduced in Section 2.2. Assume parameter priors follow normal distributions with mean $\boldsymbol{\mu}_p$ and covariance matrix $\mathbf{V}_p$. Then [33]

$$\hat{\boldsymbol{\theta}}^{MAP} = \arg\max_{\boldsymbol{\theta}} P(\boldsymbol{\theta}|\mathbf{Y}) \tag{24}$$

$$= \arg\min_{\boldsymbol{\theta}} -2\ln P(\boldsymbol{\theta}|\mathbf{Y}) \tag{25}$$

$$= \arg\min_{\boldsymbol{\theta}} J^{ML}(\boldsymbol{\theta}) + (\boldsymbol{\theta}-\boldsymbol{\mu}_p)^{\top}\mathbf{V}_p^{-1}(\boldsymbol{\theta}-\boldsymbol{\mu}_p) \tag{26}$$

$$=: \arg\min_{\boldsymbol{\theta}} J^{ML}(\boldsymbol{\theta}) + J^{p}(\boldsymbol{\theta}) \tag{27}$$

Under the above assumptions, the objective function for MAP estimation coincides with that of ML estimation, $J^{ML}(\boldsymbol{\theta})$, plus the regularization term $J^{p}(\boldsymbol{\theta})$ that accounts for prior information. Moreover, $J^{p}(\boldsymbol{\theta})$ is a quadratic function of the parameters, with the effect of adding a convex term to the original ML objective function. The smaller the prior covariance, the stronger the convexity introduced around the prior mean $\boldsymbol{\mu}_p$. As $\mathbf{V}_p$ represents the confidence in the prior mean value, this approach properly biases the estimation procedure towards $\boldsymbol{\mu}_p$. The result of the estimation, $\hat{\boldsymbol{\theta}}^{MAP}$, is therefore a balance between prior knowledge and information from the available experimental dataset. As discussed earlier in this article, lack of parameter identifiability is associated with the presence of flat regions in the objective function. The introduction of the prior term allows then to convexify such regions and, in turn, can result in bounded confidence regions. The increased convexity also improves the numerical convergence of the associated optimization.

Another method for alleviating practical unidentifiabilities is model reduction. Particular care should be taken while removing equations associated to unidentifiable parameters from the model: in closed systems such as batteries, the conservation equations must be satisfied throughout the control volume. If properly carried out, model reduction reduces the degrees of freedom in the model, thus making the parameter estimation task easier. Finally, simulation of a simpler model typically requires less time or computational power.

Finally, identifiability issues can be faced by increasing the informativity of the dataset used for parameter estimation. Practical identifiability is a property of model and training data, jointly. Identifiability of the same set of model parameters may vary, depending on the experimental data chosen for the model training. As such, the parameter identifiability is strictly associated with the design of the experiments used to collect data. For example, collecting data over a wider range of operating conditions (e.g., including charge and/or discharge data, possibly at different C-rates) is a possible way of increasing the information available in the dataset. This is particularly important when dealing with higher nonlinear systems such as lithium-ion batteries, whose dynamics can strongly depend on the operating point.

5. Conclusions

This work considers linearized and nonlinear local parameter identifiability analyses for a Multiphase Porous Electrode Theory model of commercially available Lithium Iron Phosphate batteries. The analysis focuses on parameters defining the chemical potential of active materials, as well as on conventional solid particle and electrolyte diffusivity and reaction kinetics parameters. Specifically, the dataset for the analysis consists of a single 4C synthetic discharge curve. The linearized approach suggests that the cathode's solid transport parameter is unidentifiable given the available dataset, consistent with *ab initio* predictions of fast *b*-axis diffusion in LFP nanoparticles [74,75]. All the other parameters appear to be identifiable, even though some are characterized by relatively high uncertainty. Local identifiability of parameters is further investigated by visualization of 2D confidence regions. The visualization indicates that five parameters are always locally unidentifiable, while seven are always locally identifiable. Furthermore, identifiability of these seven parameters is confirmed also in a three-dimensional identification framework. The identifiable MPET parameters for these LFP/graphite cells govern phase separation in the active materials (regular solution parameters), lithium intercalation reaction kinetics (exchange currents and film resistance), and electrolyte transport (lithium ion diffusivity), while solid diffusion parameters are not identifiable. These findings are consistent with the hypothesis that Li-ion batteries with multiphase active materials tend to be reaction limited [38,49,50,54,58–60], until electrolyte diffusion becomes rate limiting at high currents [36,37]. These findings also suggest that, in case of low or moderate currents, models can be therefore simplified by assuming infinitely fast solid diffusion and removing the corresponding governing equations from the set of DAEs. In both 2D and 3D, the shape of the nonlinear confidence regions of identifiable parameters was reasonably approximated by hyperellipsoids. This work also highlights that some the parameters defining chemical potentials may not be identifiable from the available data. Finally, this work suggests possible methods to reduce identifiability issues, such as fixing parameters, adding priors, removing equations from the model or gathering a more informative dataset (e.g., considering different operating conditions of the battery). Future developments of this work can therefore include further identifiability analysis of MPET, in case of charge data or data collected at different C-rates, as well as a full nonlinear identifiability analysis via Monte Carlo methods.

Code availability

All the software code related to this work is available online at https://github.com/GiacomoGaluppini?tab=repositories.

Funding

This work was supported by the Toyota Research Institute through the D3BATT Center on Data-Driven-Design of Rechargeable Batteries.

CRediT authorship contribution statement

Giacomo Galuppini: Conceptualization, Data curation, Formal analysis, Methodology, Software, Validation, Visualization, Writing – original draft, Writing – review & editing. **Marc D. Berliner:** Conceptualization, Formal analysis, Methodology, Writing – original draft, Writing – review & editing. **Daniel A. Cogswell:** Software, Writing – original draft, Writing – review & editing. **Debbie Zhuang:** Software, Writing – original draft, Writing – review & editing. **Martin Z. Bazant:** Funding acquisition, Project administration, Resources, Supervision, Writing – original draft, Writing – review & editing. **Richard D. Braatz:** Conceptualization, Funding acquisition, Methodology, Project administration, Resources, Supervision, Writing – original draft, Writing – review & editing.

Declaration of competing interest

The authors declare that they have no known competing financial interests or personal relationships that could have appeared to influence the work reported in this paper.

Data availability

The code will be made available on github

Acknowledgments

The authors would like to acknowledge Peter Weddle, Tyler Evans, Robert J. Kee, and Tyrone L. Vincent from Colorado School of Mines for providing some initial parameter estimates and experimental data.

Appendix. Chemical potential functions

This section describes the chemical potential functions adopted in this work to model the thermodynamics of graphite and lithium iron phosphate. Let μ_R denote the chemical potentials, $\tilde{c} = c/c_{\max}$ the dimensionless concentration in the electrode, $\bar{c}$ the average filling fraction in a particle, T the absolute temperature, and k_B the Boltzmann's constant. Moreover, let the *step down* and *step up* functions, S_d and S_u, be defined by

$$\begin{aligned} S_d(x, x_c, \delta) &= \frac{1}{2}\left(-\mathcal{T}_h\left(\frac{x - x_c}{\delta}\right) + 1\right) \\ S_u(x, x_c, \delta) &= \frac{1}{2}\left(\mathcal{T}_h\left(\frac{x - x_c}{\delta}\right) + 1\right) \end{aligned} \tag{A.1}$$

where $\mathcal{T}_h$ denotes the hyperbolic tangent function.

A.1. Graphite

The graphite chemical potential is given by

$$\mu_R = -0.12\frac{e}{k_B T} + \mu_{R_h} + \mu_{R_{nh}} + \mu_{R_{\text{ref}}} \tag{A.2}$$

with (A.3)

$$\mu_{R_{nh}} = \frac{-2k^a}{c^a_{\max}}\nabla^2\tilde{c}$$

$$\mu_{R_h} = \mu_{Lm} + \mu_{Lt} + \mu_{Rt} + \mu_{Ll} + \mu_{Rl} - 0.02 \tag{A.4}$$

where (A.5)

$$\begin{aligned} \mu_{Lt} &= \frac{-5\cdot 10^{-2}}{\tilde{c}^{0.85}} \\ \mu_{Rt} &= 10 S_u(\tilde{c}, 1.0, 0.015) \\ \mu_{Ll} &= 1.8\Omega^a_a(0.40 - \tilde{c}^{0.98}) S_d(\tilde{c}, 0.7, 4.5\cdot 10{-}2) S_u(\tilde{c}, 0.5, 5\cdot 10^{-2}) \\ \mu_{Rl} &= \left(0.4\Omega^a_a(0.74 - \tilde{c}) + 0.90\Omega^a_b - 2(1-\tilde{c})\right) S_u(\tilde{c}, 0.4, 2\cdot 10^{-2}) \\ \mu_{Lm} &= \Big[\left(40(-e^{\frac{-\tilde{c}}{0.025}}) - 2(1-\tilde{c})\right) S_d(\tilde{c}, 0.05, 5\cdot 10^{-2}) \\ &\quad + (\mathcal{T}_h(\tfrac{\tilde{c}-0.37}{0.075}) - 1) \\ &\quad + \left(\mathcal{T}_h\left(\tfrac{\tilde{c}-0.2}{0.06}\right) - 1\right) \\ &\quad + 0.1\left(\mathcal{T}_h\left(\tfrac{\tilde{c}-0.16}{0.015} - 1\right)\right)\Big] S_d(\tilde{c}, 0.5, 5\cdot 10^{-2}) \end{aligned}$$

A.2. Lithium iron phosphate

The lithium iron phosphate chemical potential is given by

$$\mu_R = -3.422\frac{e}{k_B T} + \mu_{R_h} + \mu_{R_{nh}} + \mu_{R_{ref}} \tag{A.6}$$

with

$$\begin{aligned} \mu_{R_h} &= k_B T \ln\left(\frac{\tilde{c}}{1-\tilde{c}}\right) + \Omega^c_a(1 - 2\tilde{c}) \\ \mu_{R_{nh}} &= \frac{B^c}{c^c_{\max}}(\tilde{c} - \bar{c}) \end{aligned}$$

References

[1] B. Dunn, H. Kamath, J.-M. Tarascon, Electrical energy storage for the grid: A battery of choices, Science 334 (6058) (2011) 928–935.

[2] C. Chen, F. Shang, M. Salameh, M. Krishnamurthy, Challenges and advancements in fast charging solutions for EVs: A technological review, in: IEEE Transportation Electrification Conference and Expo, 2018, pp. 695–701.

[3] N.A. Chaturvedi, R. Klein, J. Christensen, J. Ahmed, A. Kojic, Algorithms for advanced battery-management systems, IEEE Control Syst. Mag. 30 (3) (2010) 49–68.

[4] J.-M. Tarascon, M. Armand, Issues and challenges facing rechargeable lithium batteries, Nature 414 (6861) (2011) 359–367.

[5] S. Ahmed, I. Bloom, A.N. Jansen, T. Tanim, E.J. Dufek, A. Pesaran, A. Burnham, R.B. Carlson, F. Dias, K. Hardy, M. Keyser, C. Kreuzer, A. Markel, A. Meintz, C. Michelbacher, M. Mohanpurkar, P.A. Nelson, D.C. Robertson, D. Scoffield, M. Shirk, T. Stephens, R. Vijayagopal, J. Zhang, Enabling fast charging—A battery technology gap assessment, J. Power Sources 367 (2017) 250–262.

[6] U. Krewer, F. Röder, E. Harinath, R.D. Braatz, B. Bedürftig, R. Findeisen, Dynamic models of Li–ion batteries for diagnosis and operation: A review and perspective, J. Electrochem. Soc. 165 (16) (2018) A3656–A3673.

[7] M. Xu, R. Wang, P. Zhao, X. Wang, Fast charging optimization for lithium–ion batteries based on dynamic programming algorithm and electrochemical-thermal-capacity fade coupled model, J. Power Sources 438 (2019) 227015.

[8] S. Kolluri, S.V. Aduru, M. Pathak, R.D. Braatz, V.R. Subramanian, Real-time nonlinear model predictive control (NMPC) strategies using physics-based models for advanced lithium–ion battery management system (BMS), J. Electrochem. Soc. 167 (6) (2020) 063505.

[9] W. Mai, A.M. Colclasure, K. Smith, Model-instructed design of novel charging protocols for the extreme fast charging of lithium–ion batteries without lithium plating, J. Electrochem. Soc. 167 (8) (2020) 080517.

[10] X. Hu, S. Li, H. Peng, A comparative study of equivalent circuit models for Li–ion batteries, J. Power Sources 198 (2012) 359–367.

[11] C. Speltino, D. Di Domenico, G. Fiengo, A. Stefanopoulou, Comparison of reduced order lithium–ion battery models for control applications, in: Proceedings of the 48th IEEE Conference on Decision and Control held jointly with 28th Chinese Control Conference, 2009, pp. 3276–3281.

[12] C. Zou, C. Manzie, S. Anwar, Control-oriented modeling of a lithium–ion battery for fast charging, IFAC Proc. Vol. 47 (3) (2014) 3912–3917.

[13] K. Liu, T.R. Ashwin, X. Hu, M. Lucu, W.D. Widanage, An evaluation study of different modelling techniques for calendar ageing prediction of lithium–ion batteries, Renew. Sustain. Energy Rev. 131 (2020) 110017.

[14] L. Cai, J. Meng, D.-I. Stroe, J. Peng, G. Luo, R. Teodorescu, Multiobjective optimization of data-driven model for lithium–ion battery SOH estimation with short-term feature, IEEE Trans. Power Electron. 35 (11) (2020) 11855–11864.

[15] P. Khumprom, N. Yodo, A data-driven predictive prognostic model for lithium–ion batteries based on a deep learning algorithm, Energies 12 (4) (2019) 660.

[16] N. Dawson-Elli, S.B. Lee, M. Pathak, K. Mitra, V.R. Subramanian, Data science approaches for electrochemical engineers: An introduction through surrogate model development for lithium–ion batteries, J. Electrochem. Soc. 165 (2) (2018) A1–A15.

[17] K.A. Severson, P.M. Attia, N. Jin, N. Perkins, B. Jiang, Z. Yang, M.H. Chen, M. Aykol, P.K. Herring, D. Fraggedakis, M.Z. Bazant, S.J. Harris, W.C. Chueh, R.D. Braatz, Data-driven prediction of battery cycle life before capacity degradation, Nature Energy 4 (5) (2019) 383–391.

[18] Y. Li, K. Liu, A.M. Foley, A. Zülke, M. Berecibar, E. Nanini-Maury, J. Van Mierlo, H.E. Hoster, Data-driven health estimation and lifetime prediction of lithium–ion batteries: A review, Renew. Sustain. Energy Rev. 113 (2019) 109254.

[19] M. Forsuelo, Lifetime Prediction for Lithium–Ion Batteries Undergoing Fast Charging Protocols (Ph.D. thesis), Massachusetts Institute of Technology, Cambridge, Massachusetts, USA, 2019.

[20] V. Ramadesigan, K. Chen, N.A. Burns, V. Boovaragavan, R.D. Braatz, V.R. Subramanian, Parameter estimation and capacity fade analysis of lithium–ion batteries using reformulated models, J. Electrochem. Soc. 158 (9) (2011) A1048–A1054.

[21] J. Newman, W. Tiedemann, Porous-electrode theory with battery applications, AIChE J. 21 (1) (1975) 25–41.

[22] N. Jin, D.L. Danilov, P.M.J. Van den Hof, M.C.F. Donkers, Parameter estimation of an electrochemistry-based lithium–ion battery model using a two-step procedure and a parameter sensitivity analysis, Int. J. Energy Res. 42 (7) (2018) 2417–2430.

[23] S. Barcellona, L. Piegari, Lithium ion battery models and parameter identification techniques, Energies 10 (12) (2017) 2007.

[24] A. Jokar, B. Rajabloo, M. Désilets, M. Lacroix, An inverse method for estimating the electrochemical parameters of lithium–ion batteries, J. Electrochem. Soc. 163 (14) (2016) A2876–A2886.

[25] A. Raue, C. Kreutz, T. Maiwald, J. Bachmann, M. Schilling, U. Klingmüller, J. Timmer, Structural and practical identifiability analysis of partially observed dynamical models by exploiting the profile likelihood, Bioinformatics 25 (15) (2009) 1923–1929.

[26] R. Drummond, S.R. Duncan, Structural identifiability of a Pseudo-2D Li-ion battery electrochemical model, IFAC-PapersOnLine 53 (2) (2020) 12452–12458.

[27] V. Laue, F. Röder, U. Krewer, Practical identifiability of electrochemical P2D models for lithium–ion batteries, J. Appl. Electrochem. 51 (9) (2021) 1253–1265.

[28] A. Sharma, H.K. Fathy, Fisher identifiability analysis for a periodically-excited equivalent-circuit lithium–ion battery model, in: American Control Conference, 2014, pp. 274–280.

[29] J.C. Forman, S.J. Moura, J.L. Stein, H.K. Fathy, Genetic identification and fisher identifiability analysis of the Doyle–Fuller–Newman model from experimental cycling of a $LiFePO_4$ cell, J. Power Sources 210 (2012) 263–275.

[30] A.M. Bizeray, J.-H. Kim, S.R. Duncan, D.A. Howey, Identifiability and parameter estimation of the single particle lithium–ion battery model, IEEE Trans. Control Syst. Technol. 27 (5) (2018) 1862–1877.

[31] M.D. Berliner, H. Zhao, S. Das, M. Forsuelo, B. Jiang, W.H. Chueh, M.Z. Bazant, R.D. Braatz, Nonlinear identifiability analysis of the porous electrode theory model of lithium–ion batteries, J. Electrochem. Soc. 168 (9) (2021) 090546.

[32] M. Hadigol, K. Maute, A. Doostan, On uncertainty quantification of lithium–ion batteries: Application to an $LiC_6/LiCoO_2$ cell, J. Power Sources 300 (2015) 507–524.

[33] A. Gelman, J.B. Carlin, H.S. Stern, D.B. Rubin, Bayesian Data Analysis, Chapman and Hall/CRC, New York, 1995.

[34] S. Brooks, A. Gelman, G.L. Jones, X.-L. Meng (Eds.), Handbook of Markov Chain Monte Carlo, CRC Press, Boca Raton, Florida, 2011.

[35] J.V. Beck, K.J. Arnold, Parameter Estimation in Engineering and Science, John Wiley & Sons, New York, 1977.

[36] R.B. Smith, M.Z. Bazant, Multiphase porous electrode theory, J. Electrochem. Soc. 164 (11) (2017) E3291–E3310.

[37] T.R. Ferguson, M.Z. Bazant, Nonequilibrium thermodynamics of porous electrodes, J. Electrochem. Soc. 159 (12) (2012) A1967–A1985.

[38] T.R. Ferguson, M.Z. Bazant, Phase transformation dynamics in porous battery electrodes, Electrochim. Acta 146 (2014) 89–97.

[39] W. Fang, O.J. Kwon, C.-Y. Wang, Electrochemical–thermal modeling of automotive Li–ion batteries and experimental validation using a three-electrode cell, Int. J. Energy Res. 34 (2) (2010) 107–115.

[40] K.W. Baek, E.S. Hong, S.W. Cha, Capacity fade modeling of a lithium–ion battery for electric vehicles, Int. J. Automot. Technol. 16 (2) (2015) 309–315.

[41] C.M. Doyle, Design and Simulation of Lithium Rechargeable Batteries (Ph.D. thesis), University of California, Berkeley, California, USA, 1995.

[42] W.B. Gu, C.Y. Wang, Thermal-electrochemical modeling of battery systems, J. Electrochem. Soc. 147 (8) (2000) 2910–2922.

[43] J. Newman, FORTRAN Programs for Simulation of Electrochemical Systems: Dualfoil, Department of Chemical Engineering, University of California, Berkeley, 1998, http://www.cchem.berkeley.edu/jsngrp/fortran.html.

[44] M.D. Berliner, D.A. Cogswell, M.Z. Bazant, R.D. Braatz, Methods—PETLION: Open-source software for millisecond-scale porous electrode theory-based lithium-ion battery simulations, J. Electrochem. Soc. 168 (9) (2021) 090504.

[45] L. Cai, R.E. White, Mathematical modeling of a lithium ion battery with thermal effects in COMSOL Inc. Multiphysics (MP) software, J. Power Sources 196 (14) (2011) 5985–5989.

[46] M. Torchio, L. Magni, R.B. Gopaluni, R.D. Braatz, D.M. Raimondo, LIONSIMBA: A Matlab framework based on a finite volume model suitable for Li–ion battery design, simulation, and control, J. Electrochem. Soc. 163 (7) (2016) A1192–A1205.

[47] V. Srinivasan, J. Newman, Discharge model for the lithium iron-phosphate electrode, J. Electrochem. Soc. 151 (10) (2004) A1517–A1529.

[48] M. Heß, P. Novák, Shrinking annuli mechanism and stage-dependent rate capability of thin-layer graphite electrodes for lithium–ion batteries, Electrochim. Acta 106 (2013) 149–158.

[49] G.K. Singh, G. Ceder, M.Z. Bazant, Intercalation dynamics in rechargeable battery materials: General theory and phase-transformation waves in $LiFePO_4$, Electrochim. Acta 53 (26) (2008) 7599–7613.

[50] P. Bai, D.A. Cogswell, M.Z. Bazant, Suppression of phase separation in $LiFePO_4$ nanoparticles during battery discharge, Nano Lett. 11 (11) (2011) 4890–4896.

[51] D.A. Cogswell, M.Z. Bazant, Coherency strain and the kinetics of phase separation in $LiFePO_4$ nanoparticles, ACS Nano 6 (3) (2012) 2215–2225.

[52] D.A. Cogswell, M.Z. Bazant, Theory of coherent nucleation in phase-separating nanoparticles, Nano Lett. 13 (7) (2013) 3036–3041.

[53] D.A. Cogswell, M.Z. Bazant, Size-dependent phase morphologies in $LiFePO_4$ battery particles, Electrochem. Commun. 95 (2018) 33–37.

[54] J. Lim, Y. Li, D.H. Alsem, H. So, S.C. Lee, P. Bai, D.A. Cogswell, X. Liu, N. Jin, Y.-s. Yu, N.J. Salmon, D.A. Shapiro, M.Z. Bazant, T. Tyliszczak, W.C. Chueh, Origin and hysteresis of lithium compositional spatiodynamics within battery primary particles, Science 353 (6299) (2016) 566–571.

[55] H.D. Deng, H. Zhao, N. Jin, L. Hughes, B.H. Savitzky, C. Ophus, D. Fraggedakis, A. Borbély, Y.-S. Yu, E.G. Lomeli, R. Yan, J. Liu, D.A. Shapiro, W. Cai, M.Z. Bazant, A.M. Minor, W.C. Chueh, Correlative image learning of chemo-mechanics in phase-transforming solids, Nature Mater. 21 (5) (2022) 547–554.

[56] Y. Guo, R.B. Smith, Z. Yu, D.K. Efetov, J. Wang, P. Kim, M.Z. Bazant, L.E. Brus, Li intercalation into graphite: Direct optical imaging and Cahn–Hilliard reaction dynamics, J. Phys. Chem. Lett. 7 (11) (2016) 2151–2156.

[57] T. Gao, Y. Han, D. Fraggedakis, S. Das, T. Zhou, C.-N. Yeh, S. Xu, W.C. Chueh, J. Li, M.Z. Bazant, Interplay of lithium intercalation and plating on a single graphite particle, Joule 5 (2) (2021) 393–414.

[58] Y. Li, F. El Gabaly, T.R. Ferguson, R.B. Smith, N.C. Bartelt, J.D. Sugar, K.R. Fenton, D.A. Cogswell, A.L. Kilcoyne, T. Tyliszczak, M.Z. Bazant, W.C. Chueh, Current-induced transition from particle-by-particle to concurrent intercalation in phase-separating battery electrodes, Nature Mater. 13 (12) (2014) 1149–1156.

[59] K.E. Thomas-Alyea, C. Jung, R.B. Smith, M.Z. Bazant, In situ observation and mathematical modeling of lithium distribution within graphite, J. Electrochem. Soc. 164 (11) (2017) E3063–E3072.

[60] J. Park, H. Zhao, S.D. Kang, K. Lim, C.-C. Chen, Y.-S. Yu, R.D. Braatz, D.A. Shapiro, J. Hong, M.F. Toney, M.Z. Bazant, W.C. Chueh, Fictitious phase separation in Li layered oxides driven by electro-autocatalysis, Nature Mater. 20 (7) (2021) 991–999.

[61] M.Z. Bazant, Theory of chemical kinetics and charge transfer based on nonequilibrium thermodynamics, Acc. Chem. Res. 46 (5) (2013) 1144–1160.

[62] S.M. Allen, J.W. Cahn, A microscopic theory for antiphase boundary motion and its application to antiphase domain coarsening, Acta Metall. 27 (6) (1979) 1085–1095.

[63] J.W. Cahn, J.E. Hilliard, Free energy of a nonuniform system. I. Interfacial free energy, J. Chem. Phys. 28 (2) (1958) 258–267.

[64] R.A. Marcus, On the theory of oxidation-reduction reactions involving electron transfer. I, J. Chem. Phys. 24 (5) (1956) 966–978.

[65] R.A. Marcus, On the theory of oxidation-reduction reactions involving electron transfer. II. Applications to data on the rates of isotopic exchange reactions, J. Chem. Phys. 26 (4) (1957) 867–871.

[66] C.E.D. Chidsey, Free energy and temperature dependence of electron transfer at the metal-electrolyte interface, Science 251 (4996) (1991) 919–922.

[67] D. Fraggedakis, M. McEldrew, R.B. Smith, Y. Krishnan, Y. Zhang, P. Bai, W.C. Chueh, Y. Shao-Horn, M.Z. Bazant, Theory of coupled ion-electron transfer kinetics, Electrochim. Acta 367 (2021) 137432.

[68] P. Bai, M.Z. Bazant, Charge transfer kinetics at the solid–solid interface in porous electrodes, Nature Commun. 5 (1) (2014) 1–7.

[69] R. Gunawan, D.L. Ma, M. Fujiwara, R.D. Braatz, Identification of kinetic parameters in multidimensional crystallization processes, Internat. J. Modern Phys. B 16 (01–02) (2002) 367–374.

[70] A. Saltelli, M. Ratto, S. Tarantola, F. Campolongo, Sensitivity analysis for chemical models, Chem. Rev. 105 (7) (2005) 2811–2828.

[71] J.R. Leis, M.A. Kramer, Sensitivity analysis of systems of differential and algebraic equations, Comput. Chem. Eng. 9 (1) (1985) 93–96.

[72] A123 Systems official website, http://www.a123systems.com/.

[73] C. Lopez, C. Diana, G. Wozny, A. Flores-Tlacuahuac, R. Vasquez-Medrano, V.M. Zavala, A computational framework for identifiability and ill-conditioning analysis of lithium–ion battery models, Ind. Eng. Chem. Res. 55 (11) (2016) 3026–3042.

[74] D. Morgan, A. Van der Ven, G. Ceder, Li conductivity in Li_x MPO_4 (m = Mn, Fe, Co, Ni) olivine materials, Electrochem. Solid-State Lett. 7 (2) (2003) A30–A32.

[75] R. Malik, D. Burch, M.Z. Bazant, G. Ceder, Particle size dependence of the ionic diffusivity, Nano Lett. 10 (10) (2010) 4123–4127.